Supporting Information

Dihexyl-Substituted Poly(3,4-propylenedioxythiophene) as a Dual Ionic and Electronic Conductive Cathode Binder for Lithium Ion Batteries

Pratyusha Das,[1#] Billal Zayat,[1#] Qiulong Wei,[2] Charlene Z. Salamat,[3] Ioan-Bogdan Magdău,[4] Rodrigo Elizalde-Segovia,[1] Dakota Rawlings,[5] Dongwook Lee,[5] Gordon Pace,[5] Ahamed Irshad,[1] Liwei Ye,[1] Alexander Schmitt,[1] Rachel A. Segalman,[5] Thomas F. Miller III,[4] Sarah H. Tolbert,[2,3] Bruce S. Dunn,[2] Sri R. Narayan,[1] and Barry C. Thompson[1,*]

[1]Department of Chemistry and Loker Hydrocarbon Research Institute, University of Southern California, Los Angeles, California 90089-1661, USA

[2]Department of Materials Science and Engineering, UCLA, Los Angeles, California 90095, USA

[3]Department of Chemistry and Biochemistry, UCLA, Los Angeles, California 90095-1569, USA

[4]Division of Chemistry and Chemical Engineering, California Institute of Technology, Pasadena, California 91125, USA

[5]Department of Chemical Engineering, University of California at Santa Barbara, Santa Barbara, California, 93106, USA

*Email: barrycth@usc.edu

Table of Contents

Polymer Synthesis 3
Molecular Characterization 4
Fabrication and Electrochemical Characterization of PProDOT-HX$_2$ Thin Films 5
Electron paramagnetic resonance 6
Ionic and Electronic Conductivity of PProDOT-Hx$_2$ 7
GIWAXS and Ellipsometry of PProDOT-Hx$_2$ 8
Molecular Dynamics Simulations 10
Performance as an NCA Cathode Binder 16
REFERENCES 21

Polymer Synthesis

All reactions were performed under dry N_2 in oven dried glassware, unless otherwise noted. Solvents and inorganic reagents were purchased from commercial sources through VWR and used as received unless otherwise noted. Anhydrous N,N-dimethylacetamide (DMA) and cyclopentyl methyl ether (CPME) were purchased from Acros Organics and used as received. Ether, ethanol and chloroform were dried over activated molecular sieves (3Å) prior to use. NBS was recrystallized from water before use. Sodium ethoxide (NaOEt) (Alfa Aesar), Diethyl malonate (Alfa Aesar), 1-bromohexane (Alfa Aesar), $LiAlH_4$ (BeanTown Chemical), 3,4-Dimethoxythiophene (Ark Pharm), Neodecanoic acid (NDA) (Strem Chemicals), $P(t\text{-}Bu)_2MeHBF_4$ (Sigma-Aldrich) and $Pd(OAc)_2$ (> 98% TCI) were purchased and used as received. K_2CO_3 was dried at 120 °C in a vacuum oven overnight prior to use. All small molecules except compound S1 and both the monomers S3 and S4 were prepared following literature procedure.[1]

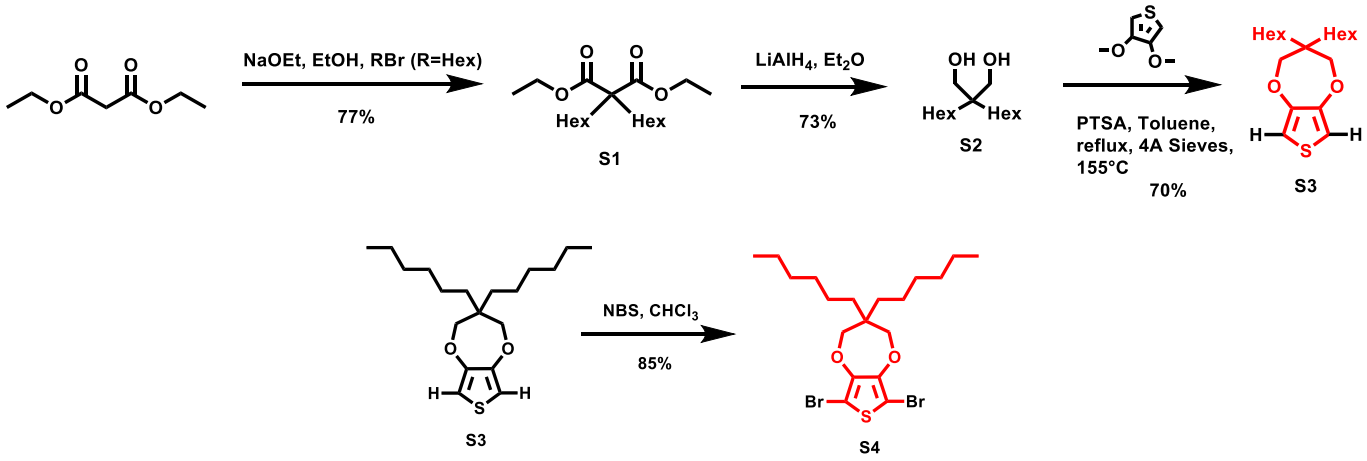

Scheme S1. Synthesis of Monomers (S3 and S4).

Synthesis of compound S1: Compound S1 was prepared following a literature procedure.[2] In a flame dried three-neck round-bottom flask equipped with an argon inlet and a condenser, Diethyl malonate (7.68 g, 48 mmol) was added to a stirred solution of NaOEt (6.80 g, 100 mmol) in 100 ml of absolute ethanol with stirring at room temperature for 30 min. Then 1-bromohexane (100 mmol) was slowly added dropwise over a period of 30 min which was followed by a mildly exothermic reaction accompanied by the formation of a white precipitate (sodium halide). The reaction mixture was refluxed overnight after which the flask was cooled to room temperature and the excess NaOEt was quenched by adding water drop wise. The organic layer was extracted with ethyl acetate, dried over $MgSO_4$ and the organic solvent was evaporated under reduced pressure. The crude product was used without further purification for the next step.

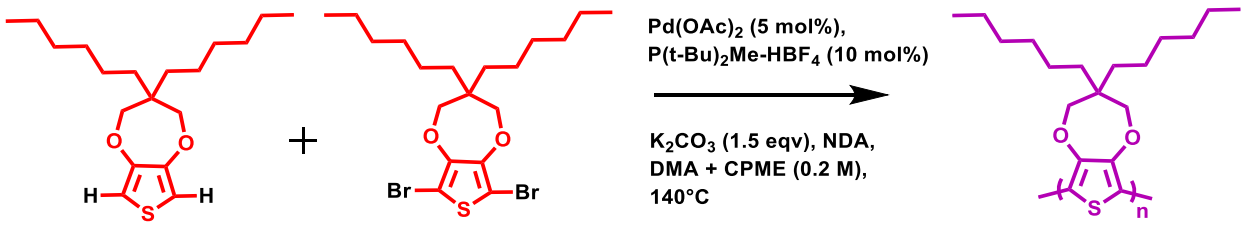

Scheme S2. Polymerization of PProDOT-Hx_2 using DArP.

Direct Arylation Polymerization (DArP) of PProDOT-Hx$_2$: PProDOT-Hx$_2$ was polymerized by modifying literature procedures.[3,4] A 100 mL oven dried high-pressure vessel with a stir-bar was capped with an inverted rubber septum and cooled under a stream of nitrogen. To this was added K_2CO_3 (995 mg, 7.2 mmol), P(t-Bu)$_2$MeHBF$_4$ (91.26 mg, 0.48 mmol), NDA (248 mg, 1.44 mmol), S3 (778.8 mg, 2.4 mmol) and S4 (1157 mg, 2.4 mmol) under nitrogen. 24 mL of 1:1 mixture of degassed CPME:DMA was added to the above mixture of reagents under nitrogen with a syringe. The vessel was degassed for 15 minutes under nitrogen before finally adding the catalyst, Pd(OAc)$_2$ (53.9 mg, 0.24 mmol) to the reaction mixture. The rubber septum was then quickly replaced with a Teflon screwcap equipped with a rubber o-ring, and the vessel was placed in a pre-heated oil bath (140 °C) for 20 hours. After cooling to room temperature, the solids were dissolved in minimum amount of $CHCl_3$ and precipitated into a cooled 10% NH_4OH/MeOH solution with rapid stirring. The polymer product was then purified using Soxhlet extraction using MeOH, hexanes, and $CHCl_3$. The chloroform fraction was concentrated by evaporation and precipitated in a chilled MeOH with rapid stirring. The polymer was obtained as a shiny purple solid in 76% yield which was then dried under vacuum overnight at room temperature. NMR data is consistent with literature reports.[1]

Molecular Characterization

All small molecules and monomer NMR were recorded at 25°C using $CDCl_3$ on either a Varian Mercury 400 MHz or Varian VNMRS-500 MHz. Polymer NMR was obtained at 25°C using $CDCl_3$ on a Varian VNMR-500 MHz. All NMR data are consistent with literature reports.[1] Number average molecular weight (M_n) and polydispersity (Đ) were determined by size exclusion chromatography (SEC) using a Waters Alliance HPLC System with 2690 Separation Module and a Waters 2410 Differential Refractometer (RI) detector, with HPLC grade chloroform ($CHCl_3$) with 0.25% triethylamine (TEA) as eluent at a flow rate of 0.5 mL/min on three Acquity APC XT Columns (45 + 200 + 450 pore sizes). The instrument was calibrated vs. polystyrene standards (200−400,000 g/mol), and data were analysed using Empower 3 software. Polymer samples were dissolved in HPLC grade $CHCl_3$ at a concentration of 3-4 mg/mL, stirred until dissolved, and filtered through a 0.45 µm PTFE filter.

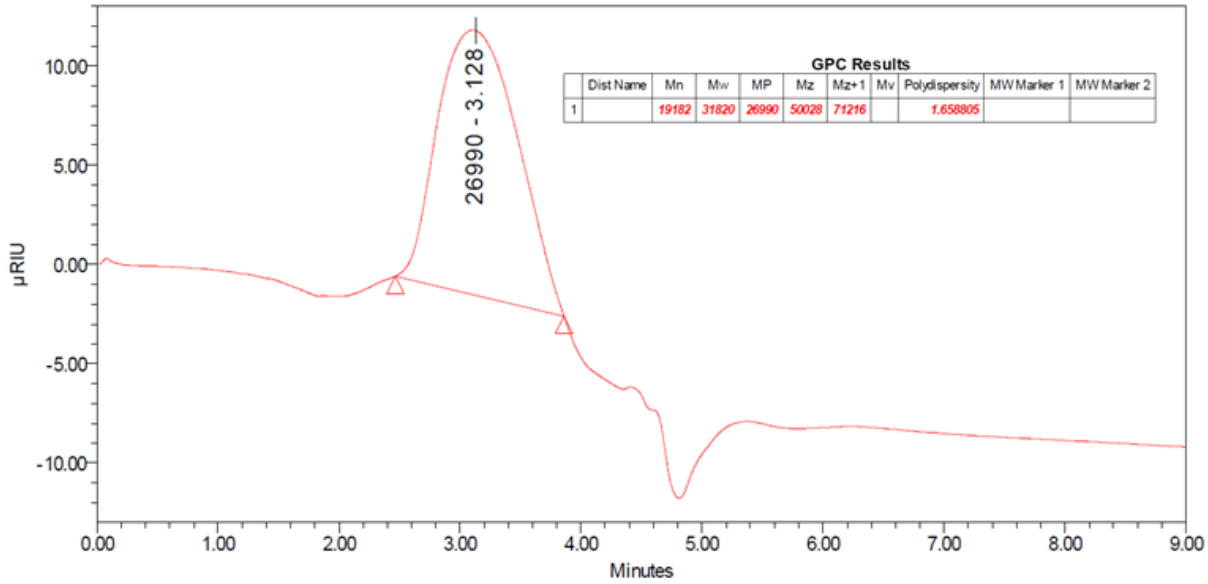

Figure S1. GPC analysis in Chloroform with calibration to a polystyrene standard: **Mn = 19,182 g mol^{-1}; Mw =31,820 g mol^{-1}; PDI = 1.6**

Fabrication and Electrochemical Characterization of PProDOT-HX_2 Thin Films

A 20 g L^{-1} solution of PProDOT-Hx_2 was dissolved in 1,2-dichlorobenzene (ODCB, Sigma-Aldrich). To prepare a thin film, 20 μL of the solution was spin-coated at a speed of 4000 rpm for 60 s onto a 1 × 1 cm^2 fluorine doped tin oxide (FTO, 7 Ω/sq, Sigma-Aldrich) coated glass. The resulting film was approximately 50 nm as measured by profilometry. The thin-film PProDOT-Hx_2@FTO was transferred into a vacuum oven at 120 °C for 4 hours and then transferred into an Ar-filled glovebox. The electrochemical doping of PProDOT-Hx_2 was tested in a three-electrode cell, thin-film PProDOT-Hx_2@FTO as the working electrode and two lithium foils as counter and reference electrodes. The utilized electrolyte is 1 M LiTFSI in ethylene carbonate (EC)/dimethyl carbonate (DMC) in a 1:1 volume ratio.

To verify the electrochemical stability of PProDOT-Hx_2, thin films of the polymer where cycled between 3.0 V and 4.2 V at 50 mV s^{-1} for 100 cycles. Figure S2 shows that the redox peaks are still very evident, thus verifying the redox stability of the polymer with a capacity retention of 60% after 100 cycles. The long-term electrochemical stability of the polymer was further tested over 500 cycles between 3.0 V and 4.0 V at 10 mV s^{-1}. Figure S3 shows good electrochemical stability with a capacity retention of 72% after 500 cycles.

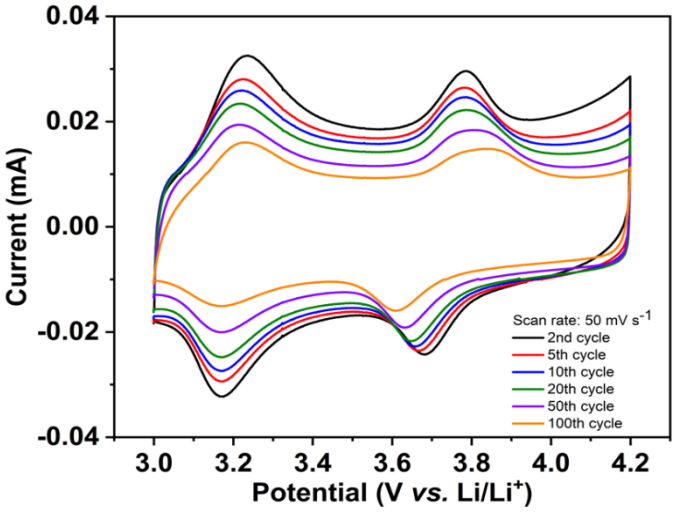

Figure S2. CV curves of PProDOT-Hx_2 thin film in 3-4.2 V at 50 mV s^{-1} for 100 cycles.

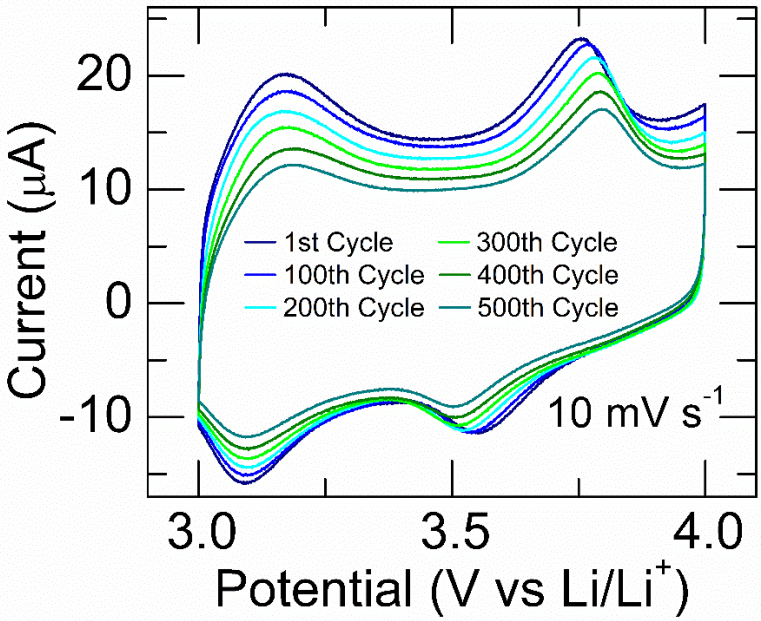

Figure S3. Long-term CV curves of PProDOT-Hx_2 thin films between 3.0 and 4.0 V at 10 mV s^{-1} with a capacity retention of 72%.

Electron paramagnetic resonance

1.0 mg/mL of PProDOT-Hx_2 solution in chloroform was dropcast on ITO-coated PET substrate under nitrogen to form EPR specimens. They were further dried in vacuum at 60 °C for 1 hour, in order to prevent mechanical weakening of the PET substrate above its glass transition temperature. After cooling down to room temperature, the PProDOT-Hx_2 films were transferred to Ar-filled glove box for electrochemical characterizations. Each film was employed as a working electrode in a beaker cell, where 2 separate pieces of Li metal served as counter and reference electrodes, respectively. The electrolyte was chosen 1.0 M $LiPF_6$ in EC:DMC (50:50 v/v). The beaker cell was sealed with parafilm to prevent evaporation of the electrolyte.

All electrochemical tests were performed under Ar. The beaker cells were firstly put under open-circuit condition for 9 hours in order to allow the cell to equilibrate, so that charge can be counted precisely during the following electrochemical tests. After the cell equilibration, repeated CV was run at 2.9 V – 4.2 V vs. Li/Li^+, with sweeping rate = 1 mV/s. Such low sweeping rate was selected to minimize influence of overpotential, so that charge count can become accurate. When CV curves from different cycles converge, the cell was allowed to rest under open-circuit condition. At this stage, spontaneous self-discharge (de-doping) of the PProDOT-Hx_2 was observed; open-circuit potential of the cell returns to 2.95 V vs. Li/Li^+ after sufficient time. At the last stage of electrochemistry, the cell was galvanostatically oxidized to a target potential, immediately followed by chronoamperometric oxidation at the same target potential. The working electrode was dismounted from the cell and rinsed with DMC 3 times. Finally, the rinsed PProDOT-Hx_2 film was dried under vacuum at room temperature for 1 hour to avoid possible de-doping at elevated temperatures. Integration of the current in CV measurements gives the total charge (Q) via equation S1 where dV/dt is the voltage sweep rate and I_{ox} represents oxidation current.[5]

$$Q = \int \frac{I_{ox}}{(dV/dt)} dV \qquad (S1)$$

Following the doping process, samples were inserted into 5 mm-diameter EPR tubes and sealed with plastic caps and parafilm in a nitrogen filled glovebox. They were then transferred outside of the glovebox and EPR spectra were measured within 1 hour. Spin concentrations were determined by comparing the normalized, integrated signal intensity of a sample with the normalized, integrated signal intensity for a series of standards at known spin concentration. 2,2-Diphenyl-picrylhydrazyl (DPPH) was used as a calibrant for determining the spin concentration. The calibrant was mixed with chloroform with known concentrations and cast onto PET substrates to obtain a known quantity of DPPH on the substrate. EPR was then measured on the standard samples as described above. See **Figure S2** for the calibration curve.

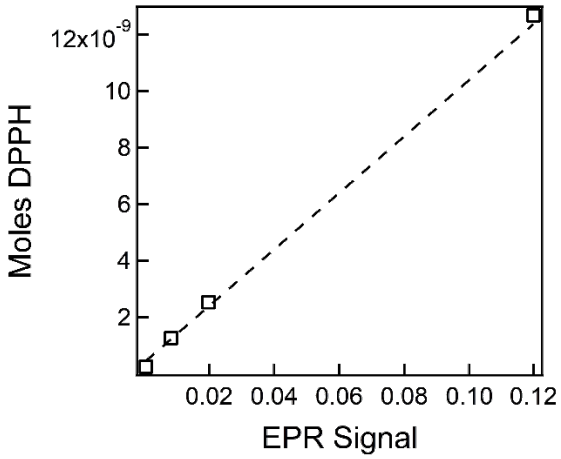

Figure S4. The normalized, integrated EPR signal intensity for a series of DPPH calibration samples with known spin concentrations.

Ionic and Electronic Conductivity of PProDOT-Hx_2

Electrode Preparation. A 20 mg/mL PProDOT-Hx_2 polymer solution was prepared by dissolving the polymer powder in 1,2-dichlorobenzene (99%, sigma aldrich). The solution was then heated at 40°C under argon for two hours to insure complete dissolving of the polymer powder in the solvent. 5 μL of the prepared solution was then spin-coated on a gold interdigitated microelectrode on a glass substrate (Metrohm Dropsens) at 1000 RPM for 30 seconds. The prepared electrode was then annealed under vacuum at 110℃ for two hours. Similarly, commercially available P3HT powder (Sigma Aldrich) was used to prepare thin films on gold interdigitated electrodes.

Electrochemical Doping. A 3-electrode cell was assembled (Figure 3b) under nitrogen to electrochemically dope the polymer and determine its ionic conductivity. The two gold microelectrodes were shorted to form the working electrode while lithium foil was used as the counter and working electrodes. 1 M LiTFSI in a 1:1 by volume mixture of ethylene carbonate and dimethyl carbonate was used as the electrolyte. To electrochemically dope the polymer, a voltage was held at the working electrode for 300 seconds to ensure complete electrochemical doping at that voltage. Cycling voltammetry scans were also performed between 3.0 V and 4.2 V vs Li/Li^+ at various scan rates to observe the electrochemical doping and de-doping process and identify the neutral-polaron and polaron-bipolaron transitions.

Ionic Conductivity Measurement. Potentiostatic electrochemical impedance spectroscopy of the 3-electrode cell was collected at the end of the potentiostatic hold at the same voltage as that of the electrochemical doping without any interruption. Impedance was collected between 100 mHz and 100 kHz with an excitation of 10 mV. The potentiostatic EIS measurement was repeated at different voltages to determine the change in ionic conductivity as a function of voltage.

The ionic resistance and ionic conductivity are represented by R_{ionic} and σ_{ionic}, respectively. The polymer film thickness is represented by h, the length and the number of the digits of the gold electrode are represented by l and N, respectively, and the distance between the gold electrodes is represented by d.

$$\sigma_{ionic} = \frac{1}{R_{ionic}} \times \frac{h}{l \times (N-1) \times d} \quad (S2)$$

Electronic Conductivity Measurement. To measure R_e accurately, the use of a different configuration for impedance measurement is necessary. In this configuration, the impedance between the two interdigitated gold electrodes is measured. Electrochemical doping of the polymer was performed in the 3-electrode configuration as before. The cell was then allowed to relax for 100 seconds to reach a steady state potential. The cell setup was then switched from a 3-electrode configuration to a 2-electrode configuration in which the gold microelectrodes are the two electrodes used (Figure 3d). EIS measurement was then performed at open circuit potential between 100 kHz and 100 mHz at an excitation of 10 mV. Electronic conductivity, σ_e, can be calculated using equation S3 where the parameters are defined as in equation S2. Note that d in this configuration is in the numerator since the current flow is between the two gold electrodes.

$$\sigma_e = \frac{1}{R_e} \times \frac{d}{l \times (N-1) \times h} \quad (S3)$$

GIWAXS and Ellipsometry of PProDOT-Hx_2

Neutral films for 2-D GIWAXS measurements were prepared on 1.5 × 1.5 cm silicon substrates. Electrochemically doped films were prepared on 1 cm × 2 cm silicon substrates with <100> orientation, resistivity of 0.001-0.005 Ω/cm, and with 100 nm of aluminum evaporated on the back-side. Measurements were performed at the Stanford Synchrotron Radiation Lightsource on beamline 11-3 using a wavelength of 0.9742 Å with an incidence angle of 0.12°. To collect the diffraction patterns, a helium chamber was used with a detector distance of 250 mm and spot size of ~150 μm. The IgorPro macro, Nika was used to calibrate and reduce the GIWAXS data. All analysis was performed in IgorPro. Each integration pattern is background corrected.

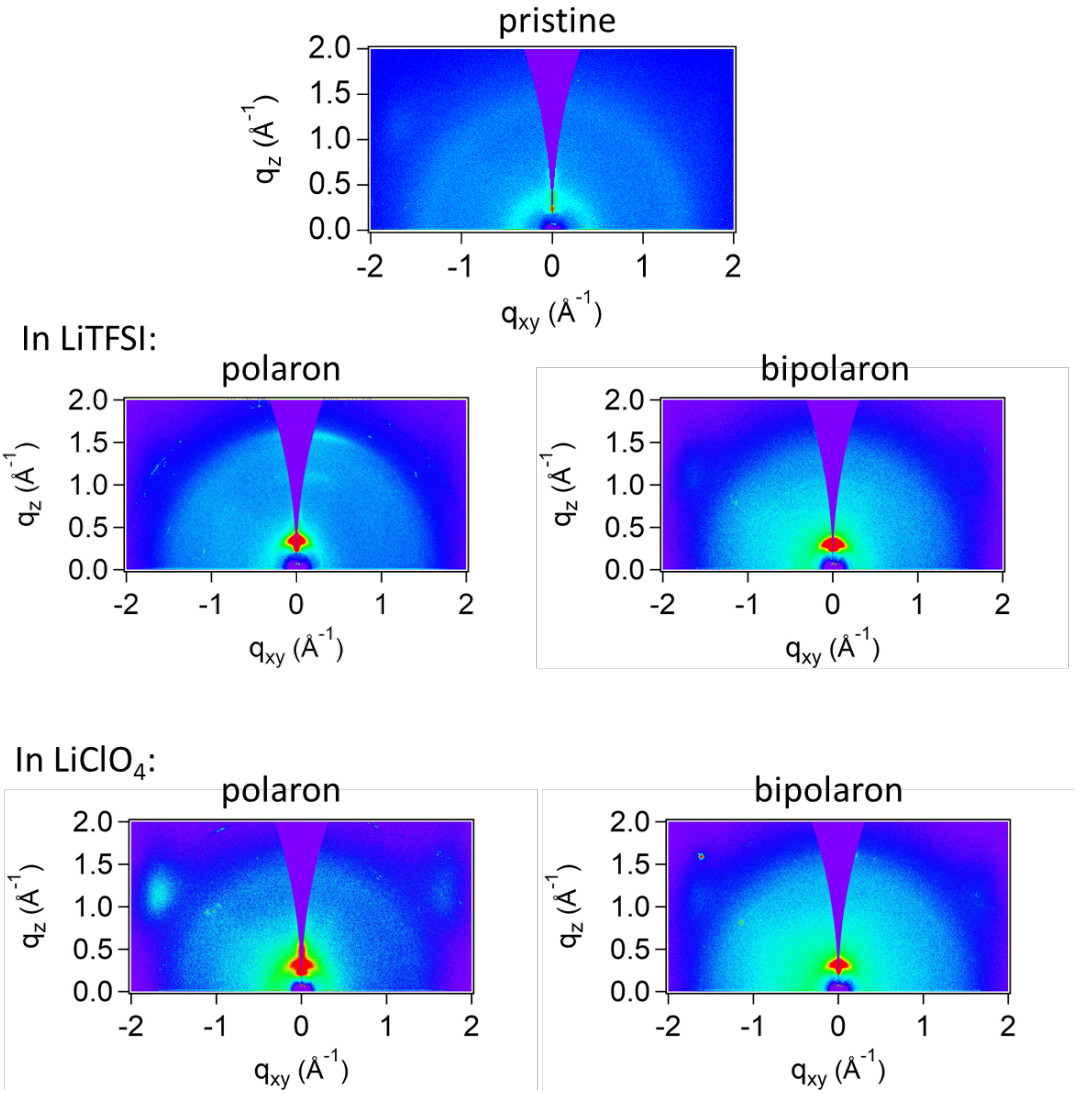

Figure S5. Representative 2-D diffractograms of PProDOT-Hx$_2$. The missing wedge of data in each image results from the grazing incidence geometry used in the experiment.

Ellipsometry was performed on a PS-1100 instrument from Semilab at room temperature. The instrument used a UV-visible CCD detector adapted to a grating spectrograph to analyze the signal reflected by the sample. The light source was a 75 W Hamamatsu Xenon lamp. Films for spectroscopic ellipsometry were prepared on 1.5 × 1.5 cm ITO substrates. Each film was measured both outside and inside of a home-built custom vial used for solvent swelling. First, the thickness of the film was measured outside of the vial as a control and then inside of the vial to ensure the thickness was the same. The films were prepared less than 1-hour prior to the measurement. The home-made vial enables *in-situ* swelling experiments with solvents that are incompatible with this elipsometeric porosimeter, such as the propylene carbonate used here. The vial has a height of 30 mm, inner diameter of 18 mm, and outer diameter of 20 mm. There are two holes 3 mm in diameter, 30 mm from the bottom of the vial that allows light to come in and out while only interacting with the film sample. Data analysis was performed using the associated Spectroscopic Ellipsometry Analyzer software.

Molecular Dynamics Simulations

Force field details. We ran all-atom MD simulations using the OPLS-AA force field[6] and the CM1A charge model.[7] All simulations were performed with LAMMPS[8] and the topology files were created using the online generator LigParGen.[9]
The potential energy surface (PES) of OPLS-AA features a bonding component given by:

$$E_{bonding} = \sum_{bonds} K_r(r - r_o)^2 + \sum_{angles} K_\theta(\theta - \theta_o)^2 + \sum_{dihedrals} \frac{1}{2}\sum_{n=1}^{4} K_n[1 - (-1)^n \cos(n\phi)] + \sum_{impropers} K[1 - \cos 2\varphi]$$

where $K_r, r_0, K_\theta, \theta_0, K_n, K$ are OPLS-AA parameters obtain with LigParGen. The generator takes coordinate inputs of up to 200 atoms, so additional post-processing was needed to extend the topology to a complete simulation box. This bonding PES was simulated in LAMMPS using the *harmonic* style for bond and angles, the *opls* style for dihedrals and *cvff* style for impropers. The non-bonding component of the PES comprises of a Coulomb and a Lennard-Jones (LJ) contribution:

$$E_{non-bonding} = \sum_{i<j} \frac{q_i q_j e^2}{r_{ij}} + 4\varepsilon_{ij}\left[\left(\frac{\sigma_{ij}}{r_{ij}}\right)^{12} - \left(\frac{\sigma_{ij}}{r_{ij}}\right)^{6}\right]$$

The pair LJ parameters were calculated from atomic LJ parameters using the geometric mixing rules:

$$\sigma_{ij} = \sqrt{\sigma_i \sigma_j}, \qquad \varepsilon_{ij} = \sqrt{\varepsilon_i \varepsilon_j}$$

where the atomic LJ parameters are summarized in Table S1 and the atom type assignment is illustrated in Figures S6d,e.

	H_{cap}	H	C_4	C_3	O_2	O_1	S
$\sigma_i(\text{Å})$	2.42	2.50	3.50	3.55	2.90	2.96	3.60
$\varepsilon_i(\text{Kcal/mol})$	0.030	0.030	0.066	0.070	0.140	0.210	0.355

Table S1. Lennard-Jones parameters for the different atom types used in the simulations.

The original CM1A charges obtained by LigParGen were symmetrized to comply with the C2 symmetry of the PProDOT-Hx_2 monomer and the final values are reported in Figures S6 a,b,c. In LAMMPS, this non-bonding PES was simulated using the *lj/cut/coul/long* pair style with a cut-off radius of 12 Å. The long-range tail correction of the LJ interaction was turned on and the pairwise energy for first-, second- and third-order bonded atoms was reweighed by 0, 0, 0.5 using the special bonds command. The long-range Ewald contribution to the Coulomb interaction was evaluated in reciprocal space using the particle-particle particle-mesh (ppm) method with a grid spacing of 10^{-4}.

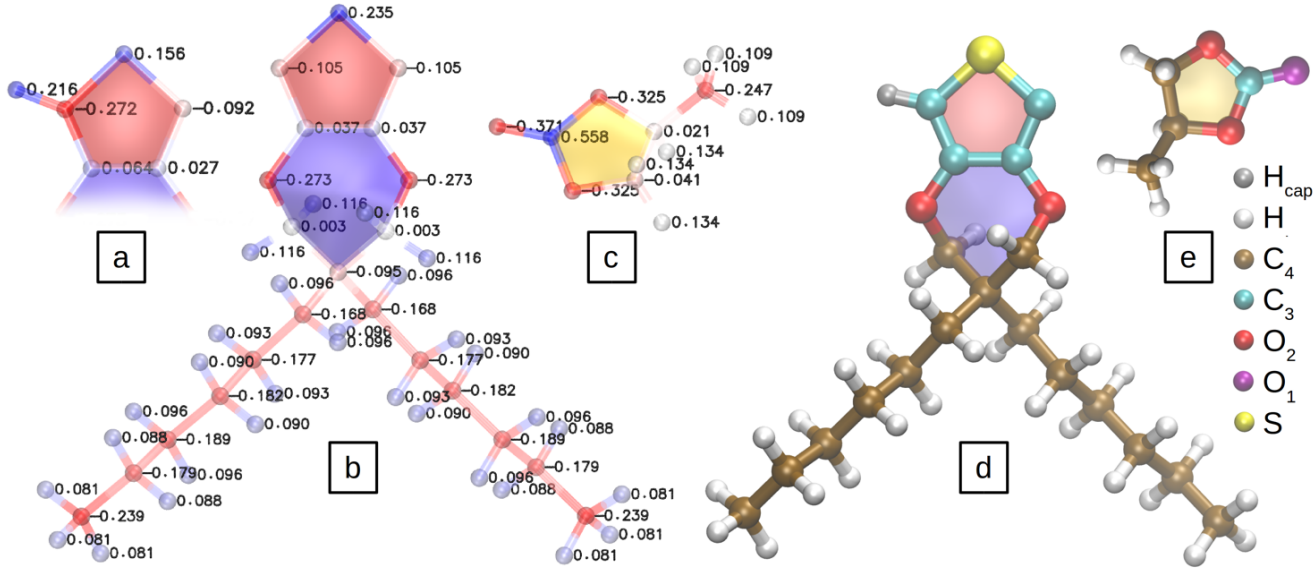

Figure S6. Force field details for PProDOT-Hx$_2$ and PC. (a, b, c) Charges used for terminal PProDOT-Hx$_2$ monomer, regular PProDOT-Hx$_2$ monomer and PC, respectively. (d, e) Atom types used for terminal/regular PProDOT-Hx$_2$ and PC.

Simulation details. All production runs were obtained using the isothermal-isobaric (NPT) ensemble with periodic boundary conditions. We used the default Nose/Hoover thermostat and barostat with damping coefficients $T_{\text{damp}} = 100$ fs and $P_{\text{damp}} = 1000$ fs. The equations of motion were propagated using the velocity-Verlet integrator with a 1 fs time-step.

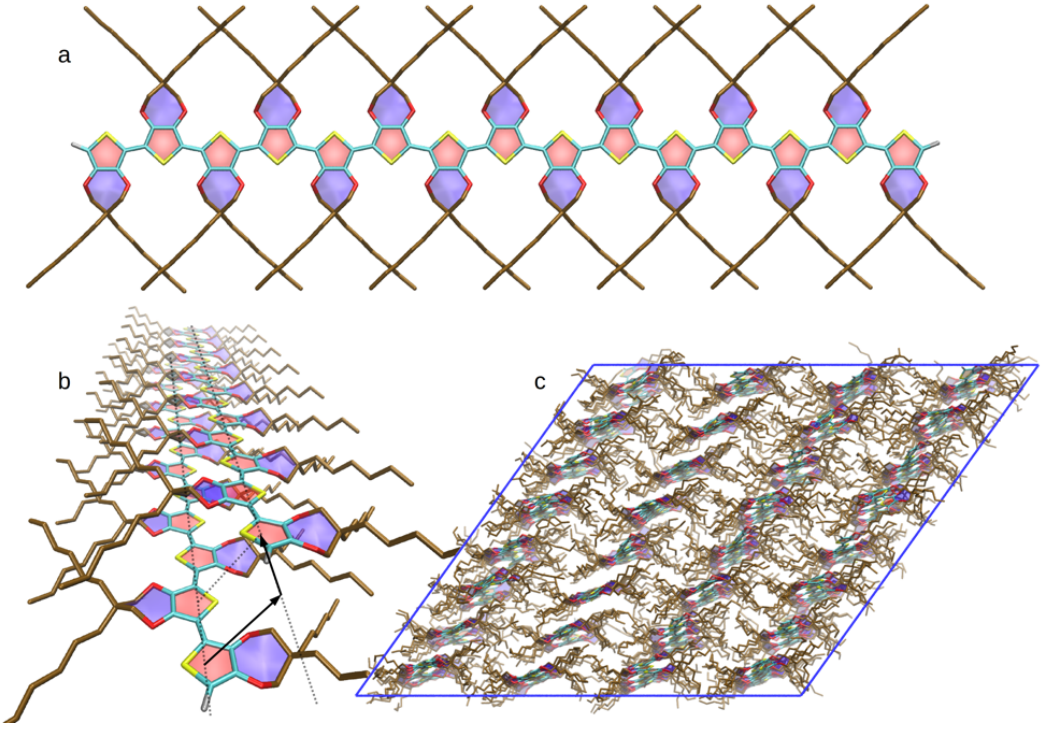

Figure S7. Setup of the crystalline simulation box. (a) The simulation comprises of 15-mers capped-off with hydrogen atoms. (b) Initially, the 15-mers are stacked by displacing every second chain one monomer over. (c) The equilibrated structure at 300 K is stable over the entire length of the simulation.

We performed crystalline and amorphous phase simulations using PProDOT-Hx$_2$ 15-mers (Figure S7). For the crystalline phase, we construct linear, planar chains and build a stacking similar to what has been reported previously in other conjugated polymers.[10] We construct a total of 4 vertical stacks of 8 15-mers each. Initially, in each stack, we displace every second chain by one monomer length (Figure S7) obtaining an ABAB stacking.[10] However, during geometry optimization we find that each displaced chain slides one more monomer, reverting back to an equivalent AA stacking. For the amorphous phase, we start by placing the polymers at very low density and run 200 ps of NVT simulation at 2000 K to create a disordered state. We then simultaneously cool and compress the simulations in an NPT ensembles to reach desired conditions.

We investigated the effects of solvent swelling by simulating binary mixtures of PProDOT-Hx$_2$ and PC as illustrated in Figure S8 and summarized in Table S2. We start with equilibrated neat structures and insert PC molecules at random in the polymer cavities, imposing a minimum distance threshold of 1 Å.

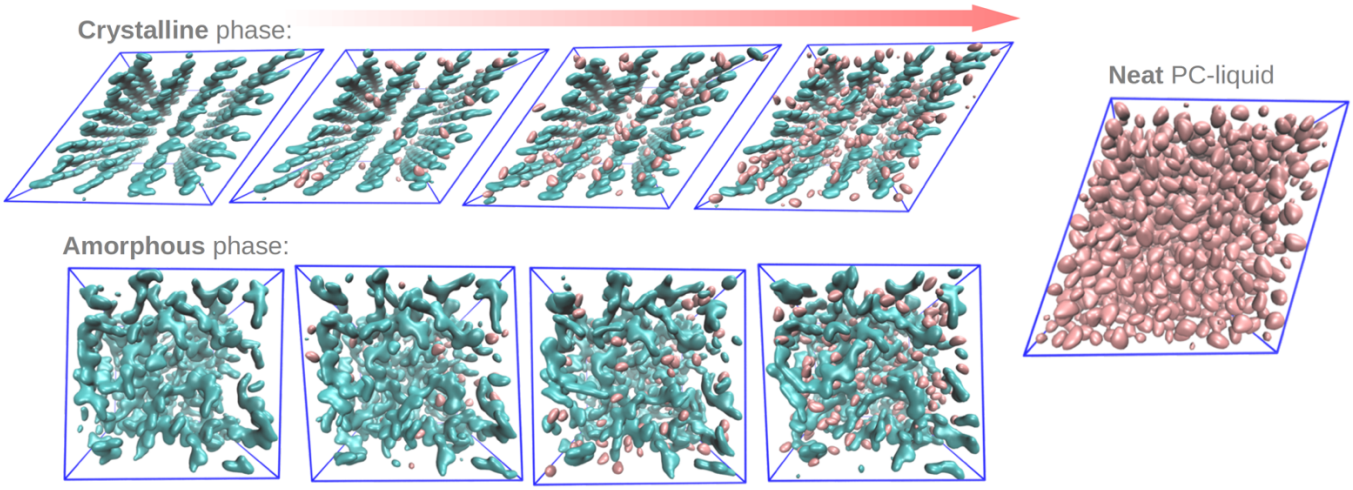

Figure S8. Binary mixtures of PProDOT-Hx$_2$ and PC with 0, 32, 96, 240 PC molecules, equilibrated at room temperature. Top: crystalline structures, bottom: amorphous structures, right: pure PC solvent.

	Neat PProDOT-Hx$_2$	Swollen PProDOT-Hx$_2$				Neat PC liquid
15-mers	4×8	4×8	4×8	4×8	4×8	0
PC molecules	0	32	96	160	240	1000
Number of atoms	25,024	25,440	26,272	27,104	28,144	13,000

Table S2. Molecular composition of the neat and swollen PProDOT-Hx$_2$ simulations.

Solvent diffusion coefficients. To ensure our swollen polymer is well equilibrated, we need to allow for sufficient diffusion of the PC molecules. We analyzed the root mean square displacement (RMSD) of the solvent molecules in the swollen crystalline phase (simulation with 160 PC molecules) at different temperatures as shown in Figure S7a. We fit $RMSD = \sqrt{6D \times t}$ to calculate the diffusion coefficients D (Figure S9b). At 500 K, after 5 ns of simulations, the PC molecules diffuse on average 3.5 nm, which is more than half the size of the simulation box $\sqrt[3]{V} \approx 6.7$ nm, allowing good equilibration. We carried out a complete set of simulations (see Table S2) at 500 K for 5 ns and then slowly cooled to 300 K for 500 ps. We then carried out a second complete set of simulations at 300 K for 5 ns.

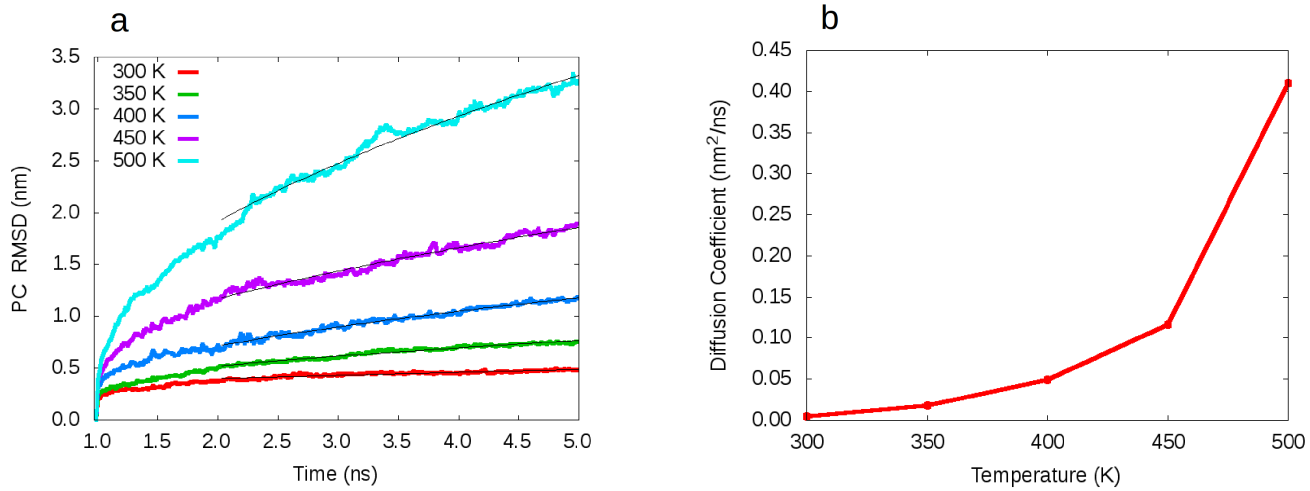

Figure S9. (a) Root mean square displacement of PC molecules in the crystalline swollen polymer at different temperatures. (b) Fitted diffusion coefficients at different temperatures.

X-Ray diffraction spectra. The finite temperature XRD was calculated from MD trajectories by averaging over instantaneous spectra and applying Gaussian smoothing to simulate disorder not captured by finite size periodic simulations. The scattering intensity I_{XRD} is computed by:

$$I_{XRD}(Q) = LP(\theta)\left\langle \sum_{hkl}^{q=Q} |F_{hkl}|^2 \right\rangle_T \text{ and } F_{hkl} = \sum_{j=1}^{N_{atoms}} f_j(q) e^{i\bar{q}_{hkl}\cdot\bar{r}_j}$$

in terms of instantaneous unit cell structure factors F_{hkl}, where $\bar{r}_j$ are the atomic positions, $f_j(q)$ are the atomic form factors and $LP(\theta)$ is the Lorentz-Polarization correction factor:

$$f_j(q) = \sum_{i=1}^{4} a_i e^{-b_i\left(\frac{q}{4\pi}\right)^2} + c\,, \qquad LP(\theta) = \frac{1+\cos^2(2\theta)}{\cos(\theta)\sin^2(\theta)}$$

where a_i, b_i and c are atom dependent fitted coefficients.[11] Q is the absolute value of the X-ray scattering vector, θ is the scattering angle, and $\bar{q}_{hkl}$ is the point in reciprocal space defined in terms of the reciprocal vectors $\bar{\beta}_i$:

$$\bar{q}_{hkl} = h\bar{\beta}_1 + k\bar{\beta}_2 + l\bar{\beta}_3, \qquad q = |\bar{q}_{hkl}|, \qquad \begin{pmatrix}\bar{\beta}_1\\ \bar{\beta}_2\\ \bar{\beta}_3\end{pmatrix}^T = 2\pi \begin{pmatrix}\bar{\alpha}_1\\ \bar{\alpha}_2\\ \bar{\alpha}_3\end{pmatrix}^{-1}, \qquad Q = \frac{2\pi}{d} = \frac{4\pi\sin(\theta)}{\lambda}$$

d is the distance between the diffraction planes and $\lambda = 0.9763$ Å is the X-ray wavelength we used in the calculations.

Pressure correction coefficients. We compare the simulated XRD spectrum of crystalline neat PProDOT-Hx$_2$ with the experimental spectrum (Figure S10) and find that the original OPLS-AA force field does not reproduce well the experimental measurement, probably due to insufficient precision of the long-range intermolecular forces. With the use of just four additional, external pressure correction parameters (Table S3) we are able to reproduce much better the experimental observation. Therefore, we extended our MD simulations to a third complete set at 300 K and under correcting-pressure.

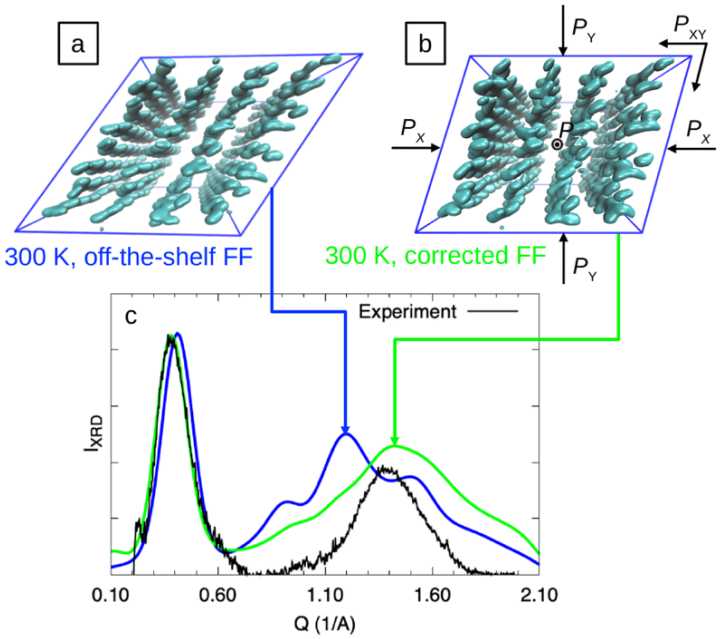

Figure S10. XRD spectrum of neat PProDOT-Hx$_2$, simulation vs experiment. (a, b) Equilibrated structures with original OPLS-AA force field vs pressure corrected simulation. (c) XRD spectra.

P_X(atm)	P_Y(atm)	P_Z(atm)	P_{XY}(atm)	P_{iso}(atm)
16.7×10^3	16.7×10^3	12.5×10^3	-1.8×10^3	15.27×10^3

Table S3. Pressure correction terms for the crystalline (P_X, P_Y, P_Z, P_{XY}) and amorphous (P_{iso}) phase.

Morphology of swollen polymer.

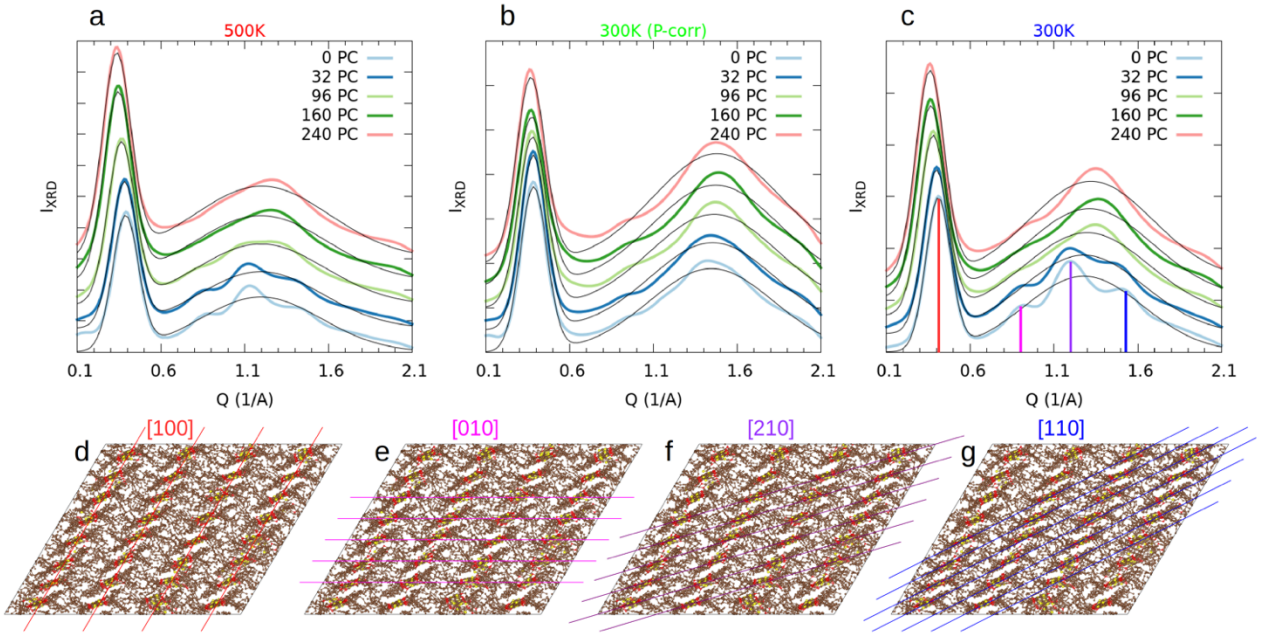

Figure S11. (a, b, c) Calculated XRD spectra as function of swelling for the three different simulation conditions. (d, e, f, g) Diffraction planes corresponding to the four lines shown in (c).

Figure S11 shows the calculated diffraction spectra for crystalline PProDOT-Hx_2 as function of PC swelling. We fit two Gaussians to each spectrum and obtained two central Q-vectors. In Figures S12a,b we report the d-spacing ($d = 2\pi/Q$) associated with these vectors. The two length scales roughly correspond to the lamellar spacing (100) and π-π stacking (010). However, on closer inspection of the uncorrected OPLS-AA simulation, we find additional subpeaks corresponding to combinations between the two symmetries. The subpeaks become broader and merge into one upon more swelling and upon increasing temperature.

1D radial distribution functions (RDFs). From each MD simulation, we compute special 1D-RDFs corresponding to the lamellar spacing and the π stacking. The two RDFs were calculated from the centers of mass of the thiophane rings: as the shortest distance from the reference ring to each neighboring lamella for the lamellar RDF (Figure S12c) and the shortest distance from the reference ring to each neighboring 15-mer within the same lamella for the π stacking RDF (Figure S12d). We then fit the peaks with Gaussians and report their positions in Figures S12e,f.

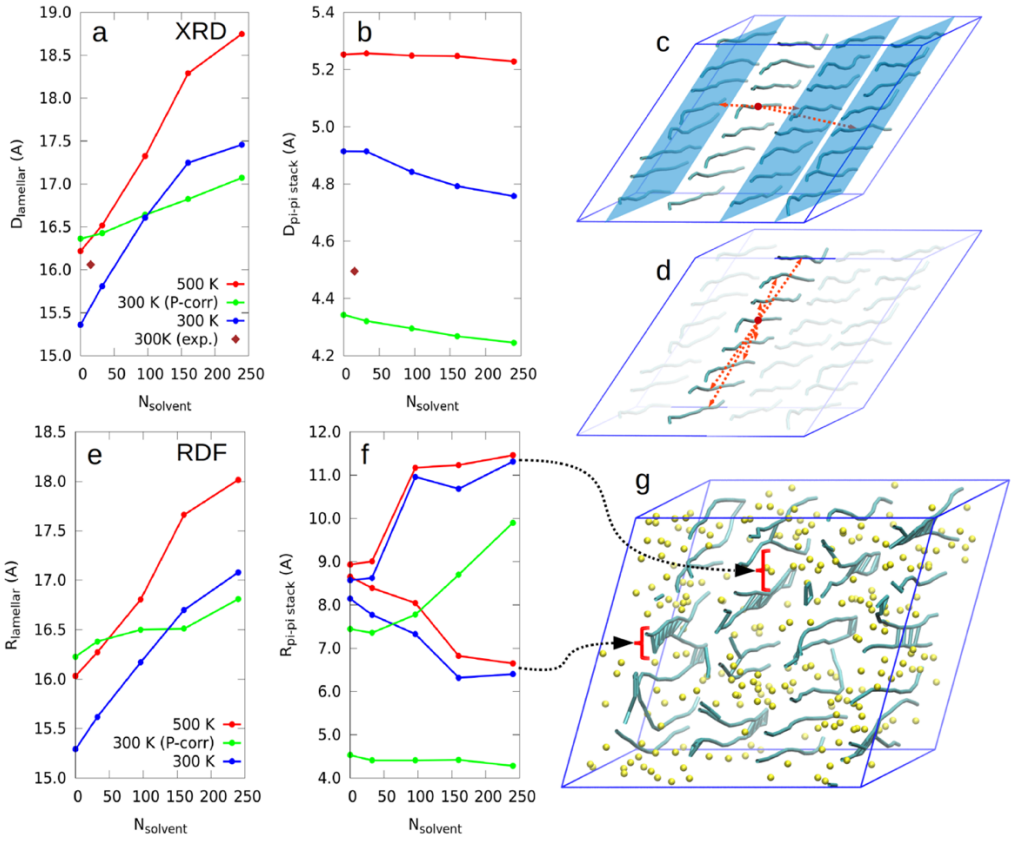

Figure S12. (a, b) The positions of the two XRD peaks fitted from simulated spectra (Figures S11a,b,c). (c, d) Calculating the 1D-RDFs: (c) lamellar and (d) π stacking. (e) Position of the first peak in the lamellar RDF and (f) position of the first two peaks in the π stacking RDF. (g) Swollen crystalline PProDOT-Hx_2 showing π stacking disorder and polymer pairing.

We find an interesting effect where the polymer chains increase the disorder of the π stacking by forming pairs (Figure S12g). The formation of such pairs breaks the symmetry of the polymer-to-polymer distance within each lamella and is made evident by the splitting of the main peak in the π stacking RDF (Figure S12f). The onset of disorder in the π stacking corresponds to the broadening and merging of the XRD subpeaks mentioned earlier. In the pressure-corrected simulation, the subpeaks are merged at all swelling conditions and the main peaks in the π stacking RDF are separated even in the neat polymer.

Distribution of Li^+ solvation sites. For each swelling configuration we carry out single ion MD simulations starting from a thermalized structure. We sample 100 different random Li^+ starting positions and let the ions diffuse for 1 ns. We then collapse all Li^+ trajectories together in a single snapshot and construct a volumetric density map, using the initial thermalized polymer configuration as reference. This results in a time-average lattice of localized density clusters corresponding to Li^+ solvation sites. We color each site based on the local character of chemical environment: polymer solvated (blue), PC solvated (red) and mix character (yellow). Additionally, we construct histograms of Li^+ binding energy, classified in a similar manner. Results are presented in the main text.

Performance as an NCA Cathode Binder

To prepare PProDOT-Hx_2-NCA electrodes, a slurry composed of NCA powders ($LiNi_{0.8}Co_{0.15}Al_{0.05}O_2$, Quallion Corp., Sylmar, CA), Super P carbon black (Sigma-Aldrich), multiwalled carbon nanotubes (CNTs, OD×ID×L: 10 nm × 4.5 nm × 3-6 μm), and the PProDOT-Hx_2/ODCB solution (20 g L^{-1}) respectively were mixed in a weight ratio of 90:3:3:4. The CNT (3 wt %) extends through the entire electrode to provide long-range electronic conductivity.[12] To prepare the PVDF-NCA control electrode, polyvinylidene fluoride (PVDF, Sigma-Aldrich) was dissolved in *N*-methyl-2-pyrrolidone (NMP, Sigma-Aldrich), and mixed with NCA, Super P carbon black, CNTs in the same ratio. For the electrodes without binder a weight ratio of 94:3:3 was employed for NCA, Super P and CNT respectively utilizing NMP as the solvent. The slurries were coated onto carbon@aluminum foil using doctor blading. The NCA electrodes were dried in a vacuum oven at 120 ℃ for 12 hours, then punched into discs with a diameter of 14 mm. Two different loadings were tested with an approximate mass loading of NCA in the electrode of about ~6 mg cm^2 and 11 mg cm^{-2}. The electrochemical performance of NCA- PProDOT-Hx_2, NCA-PVDF, and NCA without binder was tested using the same electrolyte in CR2032 coin-type cells with a Li counter electrode, Celgard 2325 separator, and 50 μL of electrolyte. The specific capacity (mAh/g) was based on the weight of the NCA in the electrode, and the capacity contribution from PProDOT-Hx_2 is negligible. Cyclic voltammetry (CV) and galvanostatic charge-discharge (GCD), were measured in a VMP-3 (Bio-Logic) potentiostat/galvanostat. For the GCD testing, different C-rates were used based on 1 C = 160 mA g^{-1} as previously reported.[12]

Initial Columbic Efficiency in the NCA electrodes:

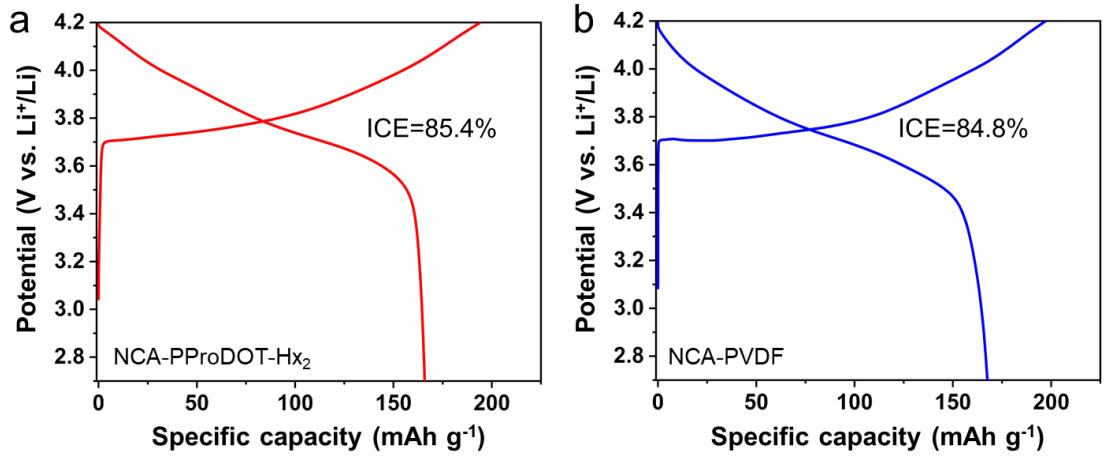

Figure S13. The initial cycle charge and discharge profiles for NCA-PProDOT-Hx_2 and NCA-PVDF electrodes at a rate of C/5.

Porosity and impedance analysis of the NCA electrodes. **Figure S14** shows the galvanostatic discharge/charge (GCD) curves at C/10 and the intervallic measurement of potentiostatic electrochemical

impedance spectroscopy (PEIS) as function of SOC (denoted with green circles) at open circuit potential (OCV) for the NCA-PProDOT-Hx$_2$ (a) and NCA-PVDF (b) cells. From the GCD curves and PEIS measurements, we can observe a remarkable lower polarization in the NCA-PProDOT-Hx$_2$ cell reflected in the narrow gap between the OCV and the galvanostatic charging/discharge curve. In contrast, the NCA-PVDF cells showed a higher voltage gap and polarization.

The impedance response for both cells has been represented in a 3D Nyquist plot as function of SOC shown below in **Figure S15**. From the 3D charts we can observe that the overall resistance is indirectly proportional to the SOC for both cells. However, the overall resistance for the NCA-PProDOT-Hx$_2$ cell is approximately 3 times lower than the NCA-PVDF cell.

To understand the impedance response as function of SOC, we have decided to utilize a well-known Transmission Line Model for a porous electrode made of cylindrical pores.[13–16] The model denotes that in the presence of a faradaic process at low frequencies (w) the real component (Zre) of the impedance response can be approximated to.

$$Z_{re} = \frac{R_{ion}}{3} + R_{ct}$$

Where R_{ion} is the Li ion mobility within the pore, and R_{ct} is the charge transfer resistance related to the electroactive surface area.

Ogihara et al.[15] have shown that R_{ion} is dependent on the electrode thickness. For our experiments, the PProDOT-Hx$_2$ and PVDF electrodes had approximately the same thickness (28 microns), therefore, we can consider the R_{ion} value to be the same for both cells. With this assumption the analysis of the Zre at low frequencies is now only dependent on the R_{ct} or the electroactive surface area of the electrode. **Figure S16** shows a comparison of the experimental Zre response as function of SOC at low frequencies for the NCA-PProDOT-Hx$_2$ cells and the NCA-PVDF cells. We can observe that the Zre of the NCA-PVDF cells is almost 3 times higher than the NCA-PProDOT-Hx$_2$ cells suggesting that the NCA-PProDOT-Hx$_2$ electrodes have an electroactive surface area 3 times higher than those made with PVDF.

These results suggest an enhanced porosity in the NCA-PProDOT-Hx$_2$ cells using this typical analysis for electrode porosity. However, we note that effects other than enhanced surface area, such as the enhanced conductivity of PProDOT-Hx$_2$ relative to PVDF could influence the measurements. Nonetheless, this analysis points to a more porous NCA-PProDOT-Hx$_2$ cells relative to NCA-PVDF.

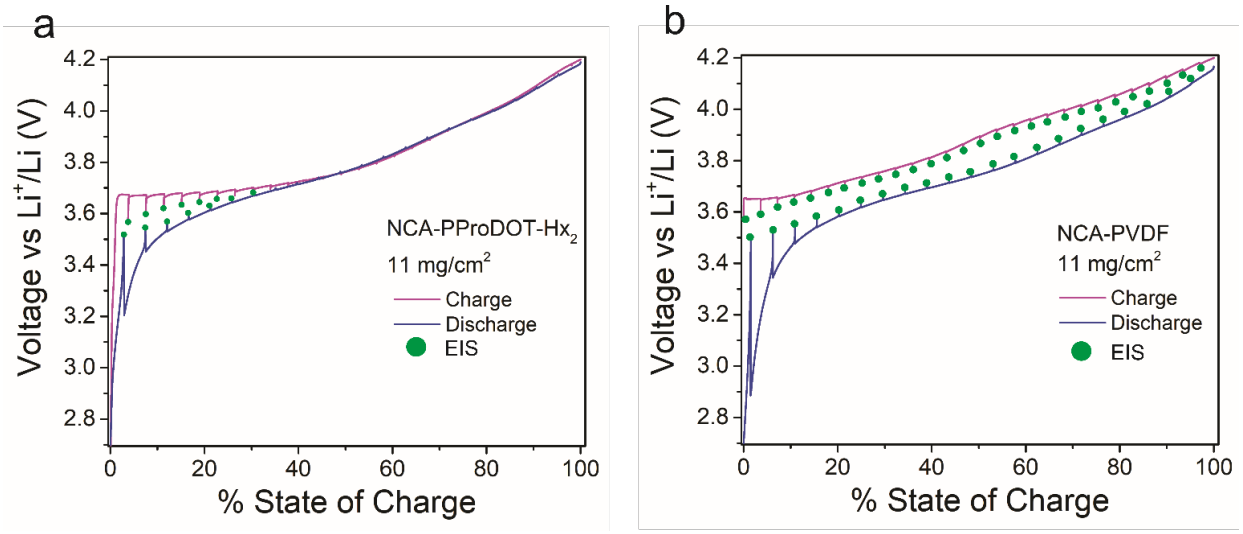

Figure S14. (a) Comparison of the charge and discharge curve of the NCA-PProDOT-Hx2 (a) and NCA-PVDF (b) at at C/10, EIS was measured as function of SOC (denoted with green circles).

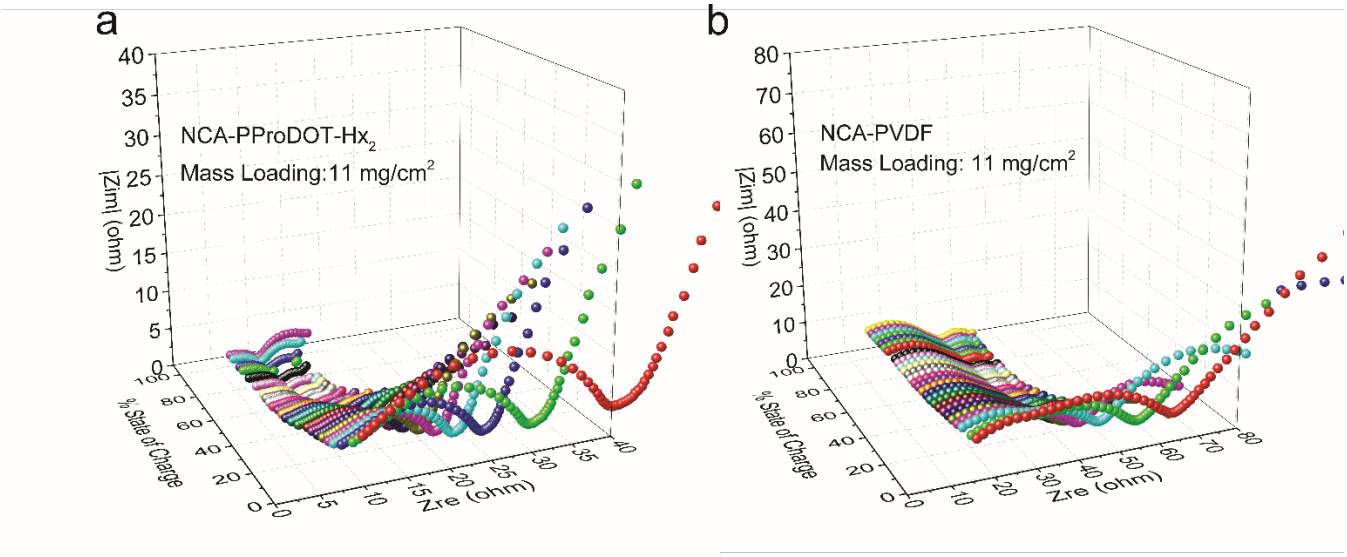

Figure S15. A three-dimensional representation of the impedance response captured in Nyquist plots as a function of the state of charge for the NCA-PProDOT-Hx$_2$ (a) and NCA-PVDF (b) cell with a mass loading of 11 mg cm^{-2}.

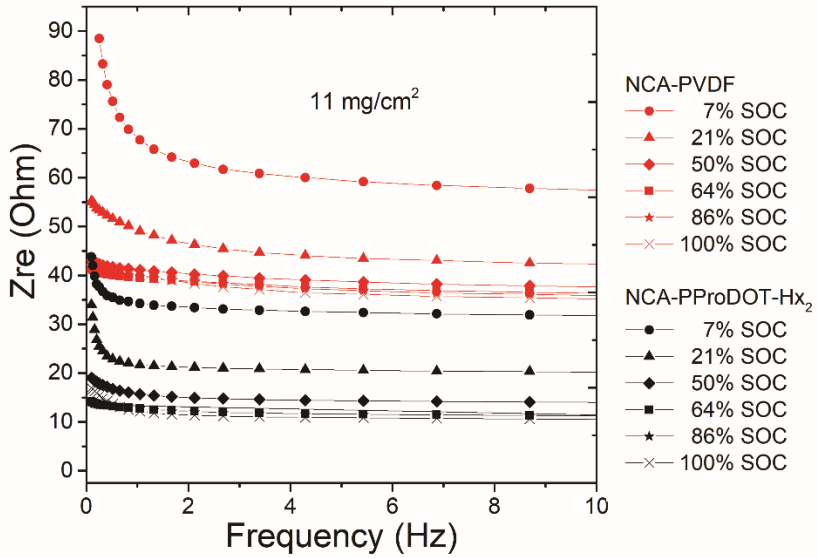

Figure S16. Real part of the impedance response agaisnt frequency (at low frequencies) as fucntion of SOC for the NCA-PProDOT-Hx$_2$ (black) and NCA-PVDF (red) cells.

NCA electrodes without binder. We have built NCA-CNT-Super P electrodes without the addition of binder in weight ratio of 94:3:3 respectively and following the same conditions to test their performance in a cell against lithium**. Figure S17** shows the rate capability comparison of the NCA-CNT-Super P (No Binder) electrodes against NCA-PVDF electrodes at two different areal mass loadings of (a) 6 mg cm^{-2} and (b) 11 mg cm^{-2}. The utilization of the binder free electrodes is lower compared to the PVDF electrodes and at higher rates the effect is magnified, suggesting a lack of connectivity within the active material, sluggish kinetics, and a lower active accessible surface area (porosity). **Figure S18** shows the corresponding galvanostatic charge/discharge curves for the NCA-CNT-Super P (No Binder) cells at (a) 6 mg cm^{-2} and (b) 11 mg cm^{-2}.

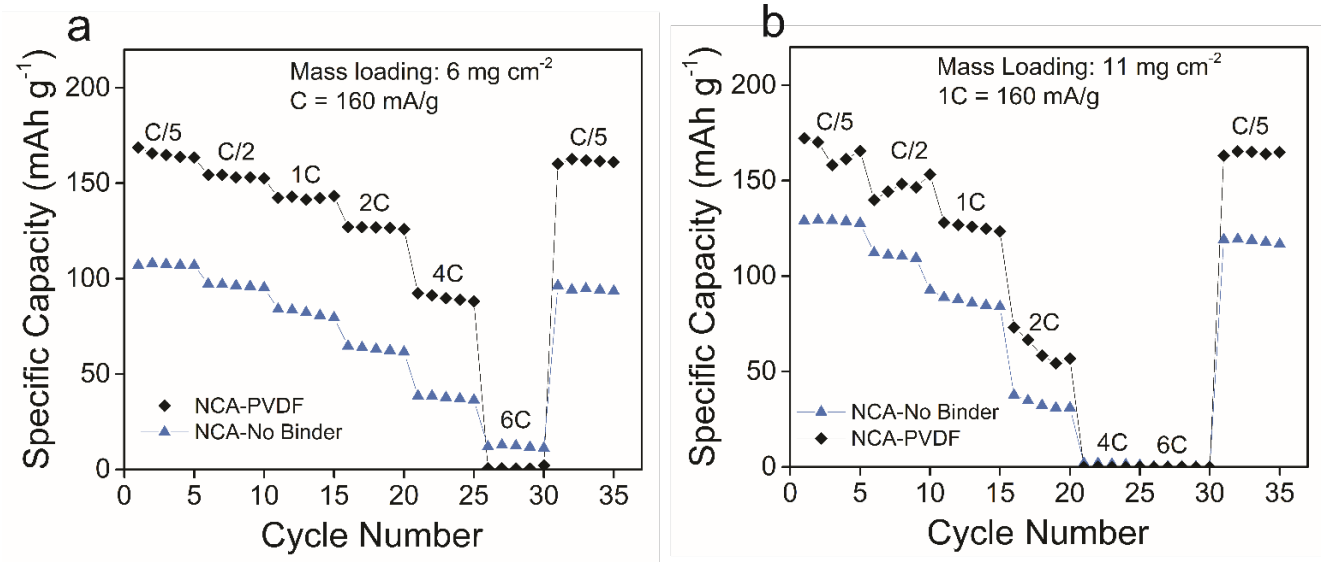

Figure S17. Rate capability comparison of the NCA-PVDF and NCA-CNT-Super P (No Binder) with an active material mass loading of (a) 6 mg cm^{-2} and (b) 11 mg cm^{-2}.

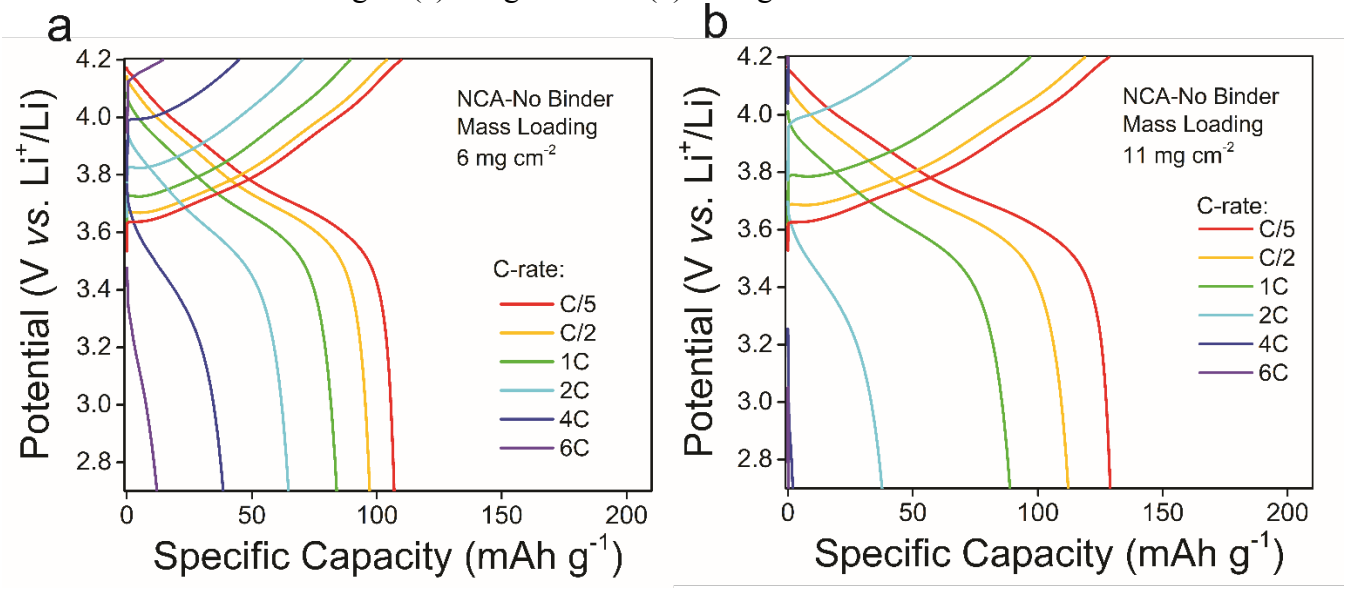

Figure S18. Galvanostatic charge-discharge (GCD) curves at various rates of the NCA-CNT-Super P (No Binder) with an active material mass loading of (a) 6 mg cm^{-2} and (b) 11 mg cm^{-2}.

NCA composite electrodes with a higher loading of 11 mg cm^{-2}. We have built NCA-PProDOT-Hx$_2$ and NCA-PVDF (control) electrodes with a higher areal loading of 11 mg/cm^2 and tested them in a cell against lithium under the same conditions in order to demonstrate the benefits of PProDOT-Hx$_2$ as a conductive additive/binder. **Figure S19** shows the rate capability comparison of the NCA-PProDOT-Hx$_2$, NCA-PVDF and NCA-CNT-Super P (No Binder) at a higher areal loading of 11 mg/cm^2. The results show how even at higher loadings of active material, the addition of PProDOT-Hx$_2$ has remarkable benefits on the cell's capacity at all rates compared to the NCA-PVDF and NCA binder free cells. **Figure S20** shows the corresponding galvanostatic charge/discharge curves for the NCA-PProDOT-Hx$_2$ (a) and NCA-PVDF (b) at various rates with an areal loading of 11 mg cm^{-2}.

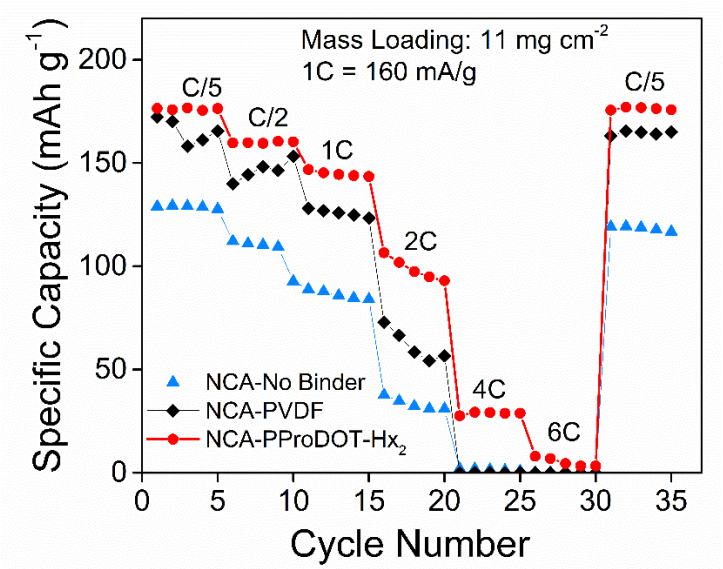

Figure S19. Rate capability comparison of the NCA-PProDOT-Hx_2, NCA-PVDF and NCA-CNT-Super P (No Binder) with an active material mass loading of 11 mg cm^{-2}.

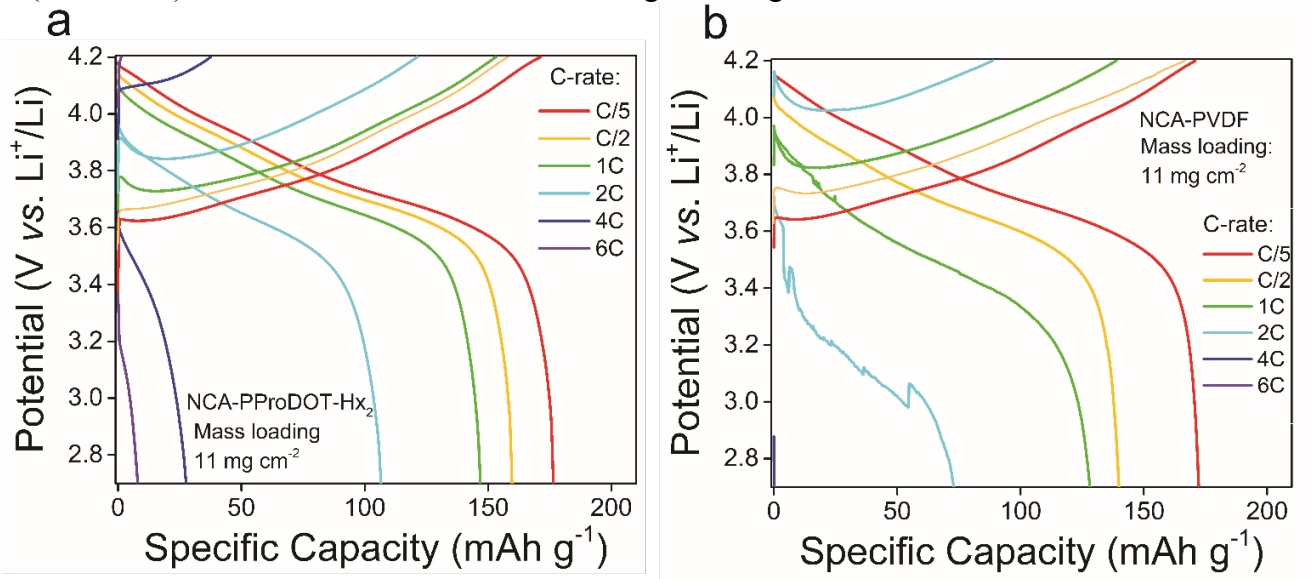

Figure S20. Galvanostatic charge-discharge (GCD) curves of the (a) NCA-PProDOT-Hx_2 and (b) NCA-PVDF at various rates with an active material mass loading of 11 mg cm^{-2}.

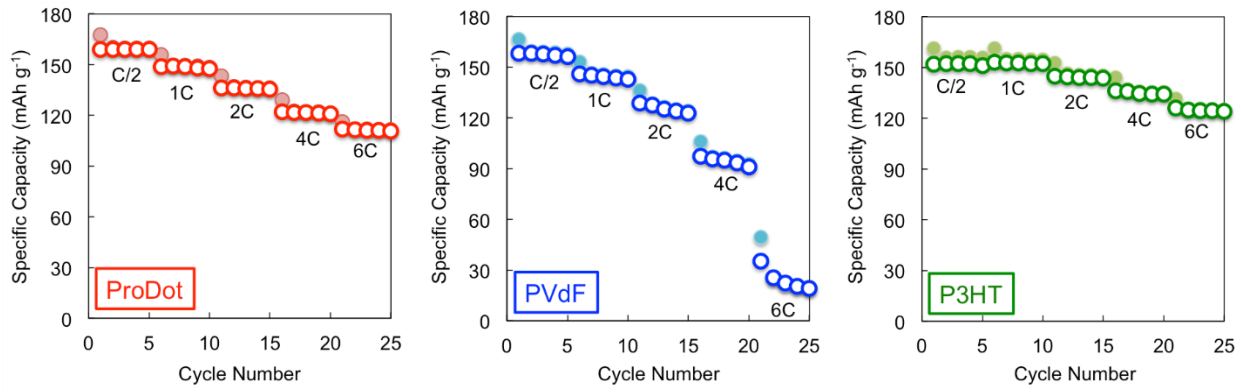

Figure S21. Rate capability comparison of the NCA-PProDOT-Hx_2, NCA-PVDF, and NCA-P3HT with an active material mass loading of ~ 6 mg cm^{-2}.

REFERENCES

(1) Reeves, B. D.; Grenier, C. R. G.; Argun, A. A.; Cirpan, A.; McCarley, T. D.; Reynolds, J. R. Spray Coatable Electrochromic Dioxythiophene Polymers with High Coloration Efficiencies. *Macromolecules* **2004**, *37* (20), 7559–7569.

(2) Chauhan, S. M. S.; Giri, N. G. Rosette Formation by Hydrogen Bonding of 5,5-Dialkylbarbituric Acids with 2-Amino-4,6-Bis[5-(4′-Aminophenyl)Porphyrinatozinc]-1,3,5-Triazines in Solution. *Supramolecular Chemistry* **2008**, *20* (8), 743–752.

(3) Pankow, R. M.; Ye, L.; Gobalasingham, N. S.; Salami, N.; Samal, S.; Thompson, B. C. Investigation of Green and Sustainable Solvents for Direct Arylation Polymerization (DArP). *Polym. Chem.* **2018**, *9* (28), 3885–3892.

(4) Zhao, H.; Liu, C.-Y.; Luo, S.-C.; Zhu, B.; Wang, T.-H.; Hsu, H.-F.; Yu, H. Facile Syntheses of Dioxythiophene-Based Conjugated Polymers by Direct C–H Arylation. *Macromolecules* **2012**, *45* (19), 7783–7790.

(5) Enengl, C.; Enengl, S.; Pluczyk, S.; Havlicek, M.; Lapkowski, M.; Neugebauer, H.; Ehrenfreund, E. Doping-Induced Absorption Bands in P3HT: Polarons and Bipolarons. *ChemPhysChem* **2016**, *17* (23), 3836–3844.

(6) Jorgensen, W. L.; Tirado-Rives, J. Potential Energy Functions for Atomic-Level Simulations of Water and Organic and Biomolecular Systems. *Proceedings of the National Academy of Sciences* **2005**, *102* (19), 6665–6670.

(7) Dodda, L. S.; Vilseck, J. Z.; Tirado-Rives, J.; Jorgensen, W. L. 1.14*CM1A-LBCC: Localized Bond-Charge Corrected CM1A Charges for Condensed-Phase Simulations. *J. Phys. Chem. B* **2017**, *121* (15), 3864–3870.

(8) Plimpton, S. Fast Parallel Algorithms for Short-Range Molecular Dynamics. *Journal of Computational Physics* **1995**, *117*, 1–19.

(9) Dodda, L. S.; Cabeza de Vaca, I.; Tirado-Rives, J.; Jorgensen, W. L. LigParGen Web Server: An Automatic OPLS-AA Parameter Generator for Organic Ligands. *Nucleic Acids Research* **2017**, *45* (W1), W331–W336.

(10) Bhatta, R. S.; Yimer, Y. Y.; Perry, D. S.; Tsige, M. Improved Force Field for Molecular Modeling of Poly(3-Hexylthiophene). *J. Phys. Chem. B* **2013**, *117* (34), 10035–10045.

(11) Brown, P. J.; Fox, A. G.; Maslen, E. N.; O'Keefe, M. A.; Willis, B. T. M. Intensity of Diffracted Intensities. In *International Tables for Crystallography*; Prince, E., Ed.; Fuess, H., Hahn, Th., Wondratschek, H., Müller, U., Shmueli, U., Prince, E., Authier, A., Kopský, V., Litvin, D. B., Rossmann, M. G., Arnold, E., Hall, S., McMahon, B., Series Eds.; International Tables for Crystallography; International Union of Crystallography: Chester, England, 2006; Vol. C, pp 554–595. https://doi.org/10.1107/97809553602060000600.

(12) Lai, C.-H.; Ashby, D. S.; Lin, T. C.; Lau, J.; Dawson, A.; Tolbert, S. H.; Dunn, B. S. Application of Poly(3-Hexylthiophene-2,5-Diyl) as a Protective Coating for High Rate Cathode Materials. *Chem. Mater.* **2018**, *30* (8), 2589–2599.

(13) de Levie, R. On Porous Electrodes in Electrolyte Solutions. *Electrochimica Acta* **1963**, *8* (10), 751–780.

(14) Ogihara, N.; Kawauchi, S.; Okuda, C.; Itou, Y.; Takeuchi, Y.; Ukyo, Y. Theoretical and Experimental Analysis of Porous Electrodes for Lithium-Ion Batteries by Electrochemical Impedance Spectroscopy Using a Symmetric Cell. *J. Electrochem. Soc.* **2012**, *159* (7), A1034–A1039.

(15) Ogihara, N.; Itou, Y.; Sasaki, T.; Takeuchi, Y. Impedance Spectroscopy Characterization of Porous Electrodes under Different Electrode Thickness Using a Symmetric Cell for High-Performance Lithium-Ion Batteries. *J. Phys. Chem. C* **2015**, *119* (9), 4612–4619.

(16) Itagaki, M.; Suzuki, S.; Shitanda, I.; Watanabe, K. Electrochemical Impedance and Complex Capacitance to Interpret Electrochemical Capacitor. *Electrochemistry* **2007**, *75* (8), 649–655.